Eurasian Journal of Physics and Functional Materials

2026, 10(4), 333-367

$BaTiO_3/SrTiO_3$ heterostructures: structure, electronic properties and photocatalytic application

A.S. Akhmedov[1], F.U. Abuova[1], A.U. Abuova[1], B.M. Satanova[1], Zh.Ye. Zakiyeva[2], U.Zh. Tolegen[1,*]

[1]L.N. Gumilyov Eurasian National University, Astana, Kazakhstan

[2]Astana International University, Astana, Kazakhstan

E-mail: t-ulzhan@list.ru

DOI: **10.32523/ejpfm.2026100402**
Received: 08 September 2026
Revised: 05 November 2026
Accepted: 16 November 2026

Perovskite oxides based on $BaTiO_3$ (BTO) and $SrTiO_3$ (STO), as well as their heterostructures, are considered highly promising materials for photocatalytic water splitting and solar fuel production owing to their tunable band structure, ferroelectric properties, and good chemical stability. In this study, a comprehensive analysis of recent literature was carried out, encompassing synthesis methods, electronic structure, and photocatalytic performance of pristine perovskites, doped systems, and heterostructures. Special attention was paid to first-principles DFT calculations of key electronic parameters, including the band gap. The review shows that pulsed laser deposition and molecular beam epitaxy (MBE) with in situ RHEED control, including hybrid MBE, provide unit-cell-level control of BTO/STO interfaces, whereas atomic layer deposition (ALD) offers low-temperature, conformal growth suitable for integration with Si. The reviewed computational and experimental data show that doping and heterostructure formation enable targeted modification of the electronic properties, significantly improving charge carrier separation, reducing the band gap, and enhancing overall photocatalytic activity. These findings highlight the potential of interface engineering in ferroelectric perovskites and may help researchers select synthesis techniques and computational approaches, since the calculated band gap depends strongly on the chosen exchange–correlation functional.

Keywords: perovskite heterostructures; $BaTiO_3/SrTiO_3$; photocatalytic water splitting; DFT calculations; hybrid functional; ferroelectric polarization; band alignment; interface engineering.

1. Introduction

The photocatalytic splitting of water using solar energy is considered one of the most promising routes for sustainable "green" hydrogen production. It enables direct conversion of solar radiation into chemical energy, bypassing the intermediate stage of electricity generation and the associated conversion losses inherent to conventional electrolysis. In contrast to electrolysers, which require high-purity water, expensive membranes and significant amounts of renewable electricity, photocatalytic systems can operate under relatively low light intensity, use abundant aqueous solutions and are potentially scalable over large areas without complex high-voltage infrastructure [1–3].

Despite these advantages, photocatalytic hydrogen production still faces serious limitations: a low solar-to-hydrogen (STH) efficiency, which for particulate photocatalysts remains around 1 % or lower (0.76 % on a 100 m^2 scale [4]), while the highest reported value of about 9 % was obtained with InGaN/GaN nanowires under concentrated sunlight [5], rapid recombination of photogenerated charge carriers, back-reaction of water formation, and insufficient long-term stability of materials in aqueous media [6]. According to the International Energy Agency's World Energy Outlook 2025, even in the Net Zero Emissions by 2050 Scenario global warming peaks at about 1.65 °C around 2050 before returning below 1.5 °C by 2100, which requires a radical acceleration in the deployment of low-emissions technologies, including low-emissions fuels such as hydrogen [7]. In this context, the development of efficient, stable and low-cost photocatalysts becomes a critical scientific and technological task. Piezo-photocatalysis is one of the strategies proposed to address these limitations; an example of the resulting enhancement in H_2 evolution is shown in Figure 1.

Among the variety of semiconductor materials, perovskite oxides based on $BaTiO_3$ (BTO) and $SrTiO_3$ (STO) and, especially, their heterostructures attract increasing attention. The choice of the $BaTiO_3/SrTiO_3$ system is not accidental. $BaTiO_3$ possesses strong ferroelectric polarization at room temperature, which creates a built-in electric field capable of effectively separating photogenerated electrons and holes. At the same time, $SrTiO_3$ offers excellent chemical stability, high photostability and a relatively favourable band-edge position for water splitting. The small lattice mismatch between the two perovskites ($\sim$2.2 %) allows the formation of high-quality coherent interfaces with minimal defect density. This combination opens unique opportunities for polarization-controlled charge separation, band alignment engineering and the realisation of piezo-photocatalytic effects (Figure 2) [9–11].

However, a number of fundamental and applied questions remain unresolved. The detailed electronic structure and charge transfer mechanisms at the BTO/STO interface, especially under the influence of spontaneous and piezoelectric polarization, are not yet fully understood. The role of surface termination, oxygen vacancies, and intentional doping in modifying band alignment and surface reactivity requires further clarification. In addition, the transition from fundamental electronic properties to real photocatalytic performance is complicated by the complex interplay between ferroelectric domain dynamics, light-induced depo-

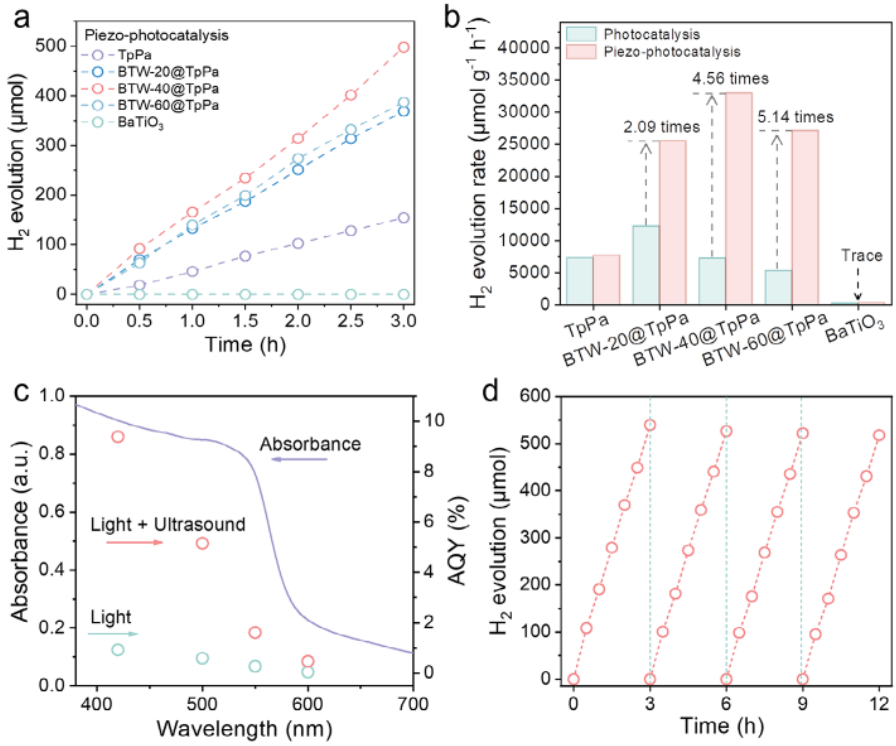

Figure 1. Piezo-photocatalytic H_2 evolution performance of $BaTiO_3$ -based piezoceramic/covalent organic framework (TpPa) hybrids [8].

larization, and surface catalytic kinetics. Long-term stability under continuous operation and scalability issues also remain important challenges.

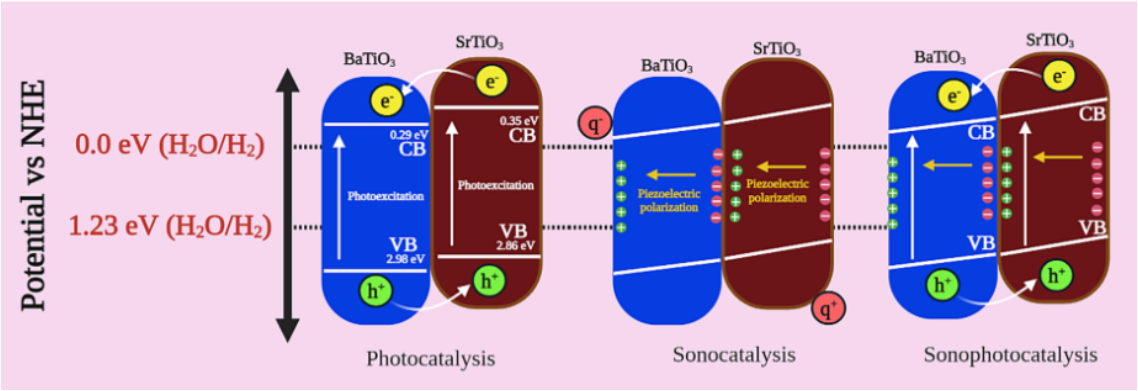

Figure 2. Photocatalytic and sonophotocatalytic mechanisms of the $BaTiO_3/SrTiO_3$ nanowire [11].

In this article, we focus on the electronic and structural properties of BTO/STO heterostructures and their influence on photocatalytic and piezo-photocatalytic performance. Particular attention is paid to the effect of ferroelectric polarization, doping strategies and interface engineering on charge separation efficiency, band-gap engineering and surface reaction kinetics. By analysing first-principles calculations together with recent experimental data, we aim to identify the most promising directions for the targeted optimisation of BTO/STO-based systems for efficient visible-light-driven hydrogen production and solar fuel technologies.

Previous reviews have addressed atomistic studies of $BaTiO_3$ as a photocatalyst for solar water splitting [12] and first-principles simulations of $SrTiO_3/BaTiO_3$ (001) heterostructures [13]. The first of them focuses on $BaTiO_3$ itself, its

doping and its heterostructures with other materials, while $SrTiO_3$ appears mainly as a reference system. The second summarizes B3PW calculations of the interface electronic structure and does not consider synthesis, doping or photocatalytic performance. In contrast, the present review is devoted specifically to the $BaTiO_3/SrTiO_3$ system. It brings together the synthesis routes of BTO/STO heterostructures, first-principles studies of pristine, defective and doped $BaTiO_3$ and $SrTiO_3$ and of their heterostructures performed with different exchange–correlation functionals, and the experimental photocatalytic and piezo-photocatalytic performance of BTO/STO heterostructures.

Following the structured literature-survey approach described in [14], the literature was collected from the Scopus, Web of Science and Google Scholar databases and from ScienceDirect and other publisher platforms. The searches combined the keywords "$BaTiO_3$ /$SrTiO_3$" with "heterostructure", "superlattice", "multilayer" and "thin film"; "$BaTiO_3$" or "$SrTiO_3$" with "doped", "vacancy", "DFT" and "first-principles"; and "$BaTiO_3$" or "$SrTiO_3$" with "photocatalytic", "piezo-photocatalytic", "water splitting" and "hydrogen". The selection includes the works that first reported each synthesis method for BTO/STO heterostructures, starting from 1989, as well as computational and experimental studies, most of which were published in 2020–2026 (74 of the 127 cited works).

2. Structure and synthesis methods

$BaTiO_3$ and $SrTiO_3$ crystals belong to the ABO_3 perovskite group, where A and B are positively charged cations, whilst O is a negatively charged anion that bonds to both cations. Within this $BaTiO_3/SrTiO_3$ heterostructure, the tetragonal phase of $BaTiO_3$, which is stable at room temperature and has the $P4mm$ space group, and the cubic phase of $SrTiO_3$, which has the space group $Pm\bar{3}m$, are considered (Figure 3). Because the lattice parameters of the two perovskites differ, lattice mismatch effects occur in heterostructures of this type. It is this lattice mismatch that gives rise to various interfacial effects, i.e. various anomalous phenomena at the boundaries between the two components of the $BaTiO_3/SrTiO_3$ heterostructure. For the room-temperature lattice parameters ($a = 3.992$ Å and $c = 4.036$ Å for tetragonal $BaTiO_3$, $a = 3.905$ Å for $SrTiO_3$), the in-plane mismatch is about 2.2 %; one of the earliest studies on $BaTiO_3/SrTiO_3$ superlattices [15] reported a mismatch of up to 3 %. Such a mismatch induces compressive in-plane strain in the $BaTiO_3$ layer, which causes $BaTiO_3$ to expand along the c axis. This was also described in subsequent studies, where thin $BaTiO_3$ films were grown on $SrTiO_3$ [16–20]. This mismatch in the $BaTiO_3$ crystal lattice relative to $SrTiO_3$, at a certain thickness of the $BaTiO_3$ layer, creates misfit dislocations and antiphase boundaries at the interface [16, 21].

Thus, the mismatch in lattice parameters between $BaTiO_3$ and $SrTiO_3$ not only leads to mechanical lattice distortion but also has a fundamental influence on the electronic structure of the interface. The distortion of $BaTiO_3$ lattice resulting from the interaction between the layers enhances spontaneous polarisation. This generates an internal electric field, which becomes a key factor in

subsequent interface effects. Lim et al. [22] established that the polarisation in the $BaTiO_3/SrTiO_3$ heterostructure has a non-uniform structure, arising from the spontaneous polarisation of the $BaTiO_3$ layer and the induced polarisation of the $SrTiO_3$ layer. In the $BaTiO_3/SrTiO_3$ heterostructure, polarisation is not merely a material property, but an active control parameter of the device. Due to the ferroelectric polarisation of $BaTiO_3$, an internal electric field is formed, and the direction of this field changes when the polarisation is switched. Changes in polarisation lead to a change in the sign of the photocurrent, which affects the drift of photogenerated carriers and the efficiency of e^-/h^+ separation [23].

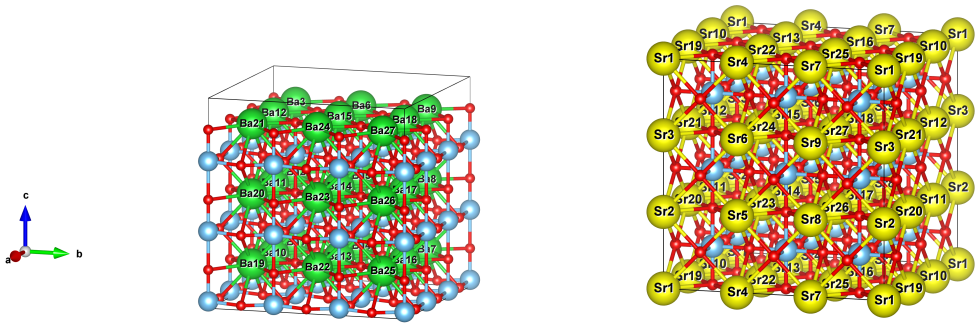

(a) BTO (b) STO

Figure 3. Crystal structure: (a) $BaTiO_3$, (b) $SrTiO_3$.

The internal electric field, which arises from the ferroelectric properties of $BaTiO_3$, is capable of radically redistributing charges in the interface region. In certain situations, this redistribution leads to an increase in the concentration of charges at the interface of the $BaTiO_3/SrTiO_3$ heterostructure. This phenomenon is known as the formation of two-dimensional electron gas (2DEG). It is a quasi-two-dimensional conducting system with high carrier mobility. In this way, the polarization field, which has a ferroelectric origin, acts not only as a mechanism for the effective separation of charge carriers, but also as a factor inducing the emergence of 2DEG-like states at the interface of the heterostructure. Unlike classical $LaAlO_3/SrTiO_3$, where the 2DEG forms as a result of a polar catastrophe [24], in $BaTiO_3/SrTiO_3$ heterostructures the 2DEG can be switched in a non-volatile manner by reversing the ferroelectric polarization [25, 26], which opens the door to additional prospects for manipulable electronic and photocatalytic processes. This is possible because of two factors: the polarisation of the ferroelectric, which allows the interface conductivity to be induced, switched and completely suppressed; oxygen vacancies, which govern the migration of the 2DEG. These features suggest a possible photocatalytic mechanism in which oxygen vacancies (V_O) and polarization-induced interfacial 2DEG states promote charge carrier separation [27–32]; its role under photocatalytic conditions remains to be verified experimentally.

To provide a clearer guide through this diversity, the main methods for synthesising $BaTiO_3/SrTiO_3$ and related heterostructures are compared in Table 1. In addition to the growth temperature and pressure, the table lists the year of the first implementation for the BTO/STO system and the key works that established or significantly advanced each method; the advantages and limitations of the methods are discussed below.

Table 1. Synthesis methods of BTO/STO heterostructures and their key parameters.

Synthesis method	First year of implementation in BTO/STO	Temperature range, °C	Pressure, mTorr	Key reference works
Pulsed Laser Deposition (PLD)	1994 [15]	600–800	5–10	[33–38]
Molecular Beam Epitaxy (MBE)	1996 [39]	500–800	10^{-4}–10^{-2}	[16, 39–47]
Magnetron sputtering	1989 [48]	500–800	1–10 (standard), 10–60 (high pressure)	[48–55]
Metal-Organic Chemical Vapor Deposition (MOCVD)	1998 [56]	600–800	10^3–10^4	[56–59]
Chemical solution deposition (CSD), sol-gel and metal-organic decomposition (MOD)	2002 [60]	300–500 (pyrolysis) 600–850 (crystallization)	ambient	[60–64]
Atomic Layer Deposition (ALD)	2014[a] [65]	225–360 (substrate) 400–600 (post-annealing)	-	[65–71]

[a] $BaTiO_3$ grown by ALD on an MBE-grown $SrTiO_3$ buffer layer.

The first successful synthesis of a $BaTiO_3/SrTiO_3$ heterostructure using the Pulsed Laser Deposition (PLD) method was carried out in 1994 [15]. In this work, the authors used a KrF excimer laser to deposit artificial superlattices on a $SrTiO_3$ (100) substrate. They demonstrated the possibility of forming epitaxial superlattices with controllable periodicity, and also showed a significant increase in dielectric permittivity compared to bulk materials. This was due to interfacial effects and epitaxial stress. In the same year, an RHEED-controlled variant of PLD was used for the first time for the atomically precise growth of $BaTiO_3/SrTiO_3$ heterostructures [33]. The use of RHEED enabled layer-by-layer growth control at the unit-cell level. This marked a breakthrough in interface sharpness. Subsequent work continued the step-by-step development of this method. Thus, in the paper [34], Si and Pt/Si were already being used as substrates. At the beginning of the 21st century, the existence of the Stranski–Krastanov growth regime was confirmed, as was the dependence of the dielectric constant on the layer period (Figure 4) [35]. The current stage of development is focused on functional design.

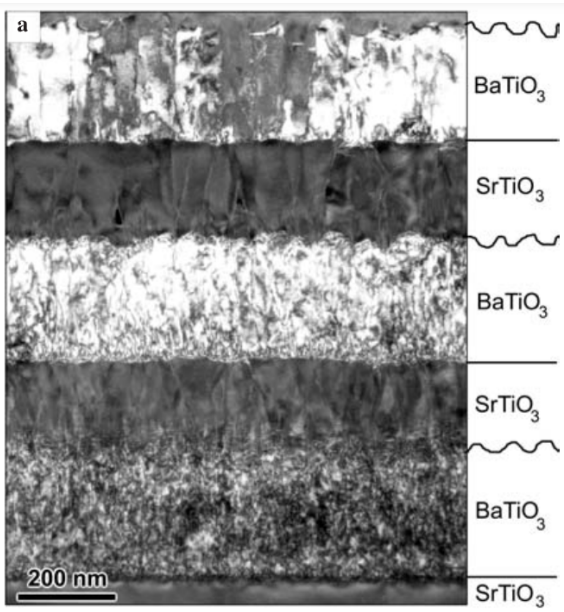

Figure 4. A cross-sectional image obtained using transmission electron microscopy (TEM) [35].

The possibility of purposefully engineering new phase states through periodicity has been demonstrated, opening up the potential for tunable materials [36].

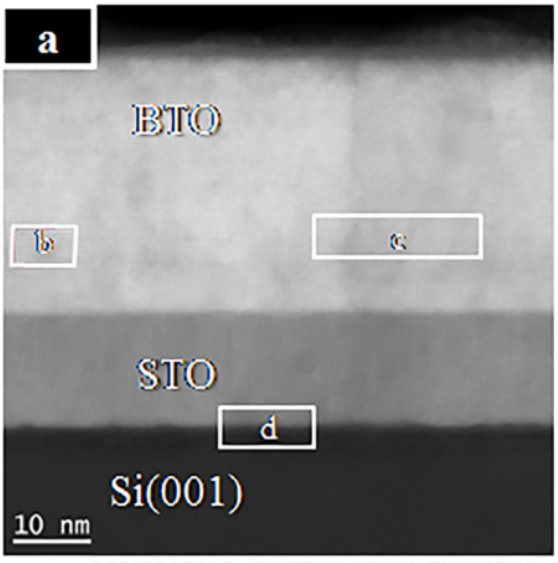

Figure 5. STEM image of BTO/STO/Si heterostructure [16].

The first key study in which the Molecular Beam Epitaxy (MBE) method was used to synthesise $BaTiO_3/SrTiO_3$ heterostructures was published in 1996 [39]. Although there was an earlier study [40], it was in this year that the layer-by-layer growth of $SrTiO_3$ and $BaTiO_3$ films was demonstrated. $SrTiO_3$ (100) was used as the substrate, onto which the films were deposited using laser molecular beam epitaxy (laser MBE, L-MBE). Following this pioneering work, a key breakthrough was achieved in [41], where short-period superlattices with unit-cell-level control of the layer thickness were demonstrated. This allowed for a more in-depth study of these heterostructures. MBE growth of $BaTiO_3$ and $BaTiO_3/SrTiO_3$ superlattices on Si, Ge and GaAs was later enabled by $SrTiO_3$ buffer layers (Figure 5) [16, 44, 46]. In parallel, the hybrid MBE method emerged, in which a

metal-organic titanium precursor (titanium tetraisopropoxide) is combined with elemental alkaline-earth sources, enabling adsorption-controlled growth with self-regulating stoichiometry [47, 72]. In recent work, hybrid-MBE has risen to prominence as a synthesis method of choice, owing to its high growth rate, minimal impurities and the ability to create freestanding films and transferable structures. Recent studies [42, 43], also highlight the ability of this method to achieve atomic precision for a wide class of perovskites, including $BaTiO_3$.

The synthesis of $BaTiO_3/SrTiO_3$ heterostructures by RF magnetron sputtering requires careful control of the parameters to achieve the required level of epitaxy, stoichiometry and defect density in the resulting structure. $SrTiO_3$ or Nb-doped $SrTiO_3$ are typically used as substrates. This method was first demonstrated for the synthesis of $BaTiO_3/SrTiO_3$ in [48]. In that work, magnetron sputtering was used to deposit c-oriented $BaTiO_3/SrTiO_3$ perovskite films, and the growth of $BaTiO_3/SrTiO_3$ bilayers was also demonstrated. This laid the foundation for the further development of this method in the context of this system. When using this method, the growth temperature is in the range $500-800\,^{\circ}C$, at a pressure (for standard cases) of 1–10 mTorr. Syntheses have also been carried out at higher pressures, [49] at 20–100 mTorr and [50] at 10–20 mTorr. High pressure thermalises negative O ions. This, in turn, reduces damage and re-sputtering. The advantages of this method are high growth rates (0.5–5 nm/min), scalability, and low cost compared to MBE and PLD. However, the synthesis mechanism itself imposes limitations in the form of potential re-sputtering and substrate etching, as well as the formation of oxygen vacancies.

The Metal-Organic Chemical Vapour Deposition (MOCVD) method is carried out at temperatures of $600-800\,^{\circ}C$ and pressures of 1–10 Torr. The first successful synthesis of a $BaTiO_3/SrTiO_3$ heterostructure was reported in [56]. In this work, the researchers grew $BaTiO_3/SrTiO_3$ superlattices on various substrates, such as $LaAlO_3$, Al_2O_3, $SrTiO_3$ and Nb-doped $SrTiO_3$. The growth rate using this synthesis method reaches 0.1–2 nm/min. The following precursors were used: for Ba and Sr - $Ba(thd)_2$ and $Sr(thd)_2$ (barium and strontium 2,2,6,6-tetramethyl-3,5-heptanedionate, respectively), for TiO_2 - $Ti(OiPr)_4$ (titanium tetraisopropoxide). This method provides good, though not atomic-level, control, unlike MBE. Its main advantages are scalability and uniformity on large substrates.

Chemical solution deposition (CSD), sol-gel and metal-organic decomposition (MOD) methods differ fundamentally from vacuum-based methods (such as MBE/PLD) [60]. This is because growth takes place at atmospheric pressure and without the use of electron beam sources, Knudsen cells or RHEED monitoring. Instead, chemical precursors, spin/dip coating and multi-step annealing are used. These methods also outperform MBE/PLD in terms of cost and scalability; however, they may exhibit high defect density and limited atomic sharpness of interfaces (interdiffusion <1 nm). In addition to these limitations, these methods, due to their step-by-step nature, involve a slower process compared to PLD.

The first application of atomic layer deposition (ALD), as well as its metal-organic variant (Metal-Organic ALD, MOALD), for the synthesis of $BaTiO_3/SrTiO_3$ heterostructures was reported in [65]. Although the $SrTiO_3$ buffer layer was obtained by MBE, the $BaTiO_3$ itself was grown by ALD at a relatively low

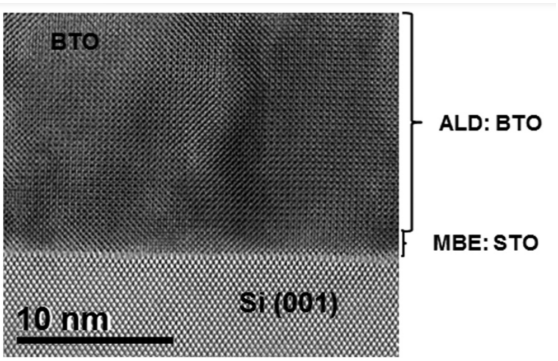

Figure 6. STEM image of ALD-grown BTO [65].

temperature of 225 °C using metal-organic precursors (Figure 6). This method allows heterostructures to be produced with atomic-layer control of film thickness at low temperatures, surpassing traditional methods in terms of conformality and integration with Si. Furthermore, such heterostructures are characterised by high dielectric permittivity values with low loss and leakage levels.

3. Electronic properties

3.1 Computation of single systems

A key starting point in the study of perovskite materials in photocatalysis is a detailed analysis of their pure, undoped structures. It is precisely through such models that we can understand the material's "fundamental" behavior: how its electronic structure is organized, how wide its bandgap is, and how intrinsic defects influence the processes of charge generation, separation, and recombination? Of particular interest are vacancies—primarily oxygen vacancies, as well as vacancies in the A- and B-sites of cations—since they frequently occur in real synthesized samples and can either improve or impair photocatalytic properties. Table 2 summarizes published calculations for stoichiometric perovskite structures and structures containing various types of vacancies. For each study, it lists the computational method and the main reported results on the band gap, defects and photocatalytic activity.

Table 2. Calculation of single systems.

System	Methods	Main results
$BaTiO_3$ with Ba and Ti vacancy [73]	VASP, DFT framework, $2 \times 2 \times 2$ supercell	The Ba/Ti ratio influences tetragonality. Ti vacancies cause a greater lattice expansion than Ba vacancies. Oxygen vacancies are necessary to maintain charge balance. Charge density equalizes at Ti vacancy sites

$BaTiO_3$ with oxygen vacancies [74]	DFT (Materials Studio 2017), GGA-PBE, 400 eV cutoff, $3 \times 3 \times 3$ k-mesh	Oxygen vacancies reduce band gap from 3.058 eV to 2.717 eV. Enhanced charge transfer between Ti and O vacancy. CO production: 6.41 μmol g^{-1} (light only), 9.17 μmol g^{-1} (light + ultrasound)
$BaTiO_3$ [75]	VASP 5.4.4, GGA-PBE, DFT-D3	In-plane polarisation enhances the hydrogen evolution reaction compared with out-of-plane polarisation. Surface roughness affects the reactivity of oxygen. The optimal O 2p band centre correlates with improved hydrogen evolution activity. A catalytic cycle of ferroelectric polarisation is proposed
$BaTiO_3$ [76]	Quantum ESPRESSO, DFT+U (U=4 eV for Ti_d), 320 eV cutoff, $4 \times 4 \times 1$ k-mesh	Upward polarization reduces the work function and lowers the energy barrier for the hydrogen evolution reaction. Upward-polarized surfaces exhibit lower reaction barriers. TiO_2-terminated slabs are the most stable; polarization dynamically switches electrocatalytic surfaces
Cubic ($Pm\bar{3}m$) and two tetragonal ($P4\,mm$, $P4/mmm$) phases of $BaTiO_3$ [77]	GGA-PBE + U approximation	Systematic U (Hubbard U) correction improves band gap accuracy for cubic and tetragonal BTO phases
$SrTiO_3$ with oxygen vacancies [78]	Neural Network Potentials (NNP) trained on DFT data	Oxygen vacancies act as n-type dopants, introducing defect levels into the band gap. DFT-calculated static properties, such as the density of states, band structure and formation energy, have been investigated. Dynamics and thermodynamics can now be studied by NNP-based molecular dynamics

$BaTiO_3$ [79]	DFT+U+V with self-consistent determination of Hubbard parameters (extended ACBN0 method). Comparison with LDA, PBEsol and HSE06	The standard DFT+U method predicts an incorrect centre-symmetric ground state for BTO and underestimates the polar distortions. The inclusion of U+V intersite terms corrects this, yielding properties close to those of HSE06, but $\sim$30 times faster. This makes the approach attractive for predicting band gaps and band alignment in large ferroelectric heterostructures
$PbTiO_3$ [80]	DFT (VASP), HSE06 for electronic structure, calculation of piezopotential and *OH/*H adsorption	Bulk and few-layer PTO exhibit opposite trends in the change of the band gap (E_g) under strain. A voltage-dependent piezopotential has been observed, which describes the driving force behind piezocatalysis. The adsorption of *OH and *H is enhanced under both tensile and compressive stress
$BaTiO_3$ [81]	GGA, mBJ-GGA	Electronic band structure calculations using mBJ-GGA reveal a direct bandgap width of approximately 2.7 eV
$BaTiO_3$ at room temperature [82]	VASP, PBE+U (U = 2.6 eV on Ti 3d) and HSE06, AIMD at 300 K, $3 \times 3 \times 3$ supercell (135 atoms)	PBE+U gives an indirect band gap of 1.94 eV, HSE06 a gap of 3.56 eV at Γ. Thermal motion of the atoms red-shifts the absorption threshold by about 0.5 eV, which gives an estimated threshold of 3.2 eV, in agreement with experiment. The simulated photoluminescence spans 1.8–2.8 eV

The analyzed studies have convincingly demonstrated that the structural and

electronic properties of ferroelectric perovskites (primarily $BaTiO_3$ and $PbTiO_3$) are determined by the complex interplay of cation ratio, point defects, and spontaneous polarization. Oxygen vacancies act as n-type dopants, significantly narrowing the bandgap (from 3.058 to 2.717 eV), introducing defect levels, and enhancing charge transport, which leads to a significant increase in photocatalytic activity, particularly an increase in CO yield [74, 78]. Titanium vacancies cause a stronger lattice expansion compared to barium vacancies and require the presence of oxygen vacancies to maintain electrical neutrality. Accurate treatment of electronic correlations (especially via extended DFT+U+V or mBJ-GGA) is critically important: standard DFT+U yields an erroneous centrosymmetric state and underestimates polar distortions, whereas more advanced approaches improve the prediction of the band gap, band alignment and material dynamics [79, 81]; even so, the mBJ-GGA value of $\sim$2.7 eV remains below the experimental band gap of $BaTiO_3$ (about 3.3 eV [83]). Finite temperature also matters: room-temperature AIMD shows that thermal motion lowers the HSE06 absorption threshold of $BaTiO_3$ by about 0.5 eV, to about 3.2 eV, close to the experimental value [82]. The direction and magnitude of ferroelectric polarization play an equally important role. In-plane polarization significantly outperforms out-of-plane polarization in terms of hydrogen evolution reaction efficiency, while upward polarization reduces the work function and the HER energy barrier. Dynamic polarization switching allows for active control of catalytically active surfaces, and in piezocatalysis, both stretching and compression enhance the adsorption of *OH and *H, although bulk and thin-film $PbTiO_3$ samples exhibit opposite trends in piezopotential changes. Surface roughness and the optimal position of the O 2p-band center also correlate with increased catalytic activity [75, 80]. Thus, the targeted introduction of oxygen vacancies combined with the control of ferroelectric polarization opens up broad possibilities for fine-tuning the electronic and catalytic properties of perovskite materials. The results obtained lay a solid foundation for the development of highly efficient ferroelectric catalysts for photo-, electro-, and piezocatalysis, as well as for promising energy storage and energy conversion devices.

3.2 Computation of doped systems

Now that we have examined the behavior of pure perovskites and the role of intrinsic defects, it makes sense to move on to one of the most common and effective methods for their targeted modification: doping. The introduction of foreign atoms allows for fine-tuning the electronic properties of the material, reducing charge recombination, shifting the absorption edge into the visible region, and increasing stability under the influence of light and moisture. In photocatalysis, this is particularly important, as it directly affects the efficiency of pollutant decomposition, hydrogen generation, or carbon dioxide reduction. Table 3 summarizes published calculations on doped perovskite structures. It lists the dopants, the computational methods and the reported changes in electronic structure and photocatalytic performance.

Table 3. Calculation of doped systems.

System	Methods	Main results
La-doped $BaTiO_3$ [84]	Materials Studio DFT, GGA-PBE, Birch-Murnaghan EOS, 340 eV cutoff	Lattice constant: 4.034 Å (pure), 3.971 Å (La-doped); La_{5d} states alter the structure of the conduction band; the refractive index varies from 2.598 to 2.482
Mo-doped $BaTiO_3$ [85]	VASP, GGA-PBE, 500 eV cutoff	Doping with molybdenum narrows the bandgap to 1.27 eV; Ti_{3d}–Mo_{4d} hybridisation shifts the lower boundary of the conduction band downwards; H_2 evolution rate: 63 $mmol\,g^{-1}\,h^{-1}$ (2 at.% Mo) compared with 35 $mmol\,g^{-1}\,h^{-1}$ (pure material)
Cs-doped $BaTiO_3$ [86]	Plane-wave pseudopotential, PBE, DFT+U (U=4 eV for Ti_d)	Pure BTO: indirect gap 2.513 eV, lattice 4.034 Å; Cs doping converts to direct band gap; 0.13% Cs shows highest visible absorption
$BaTiO_3$ codoped with TM and X (where TM = V, Nb, Ta, Mo and W, X = N and C) [87]	VASP, GGA-PBE, HSE06 for selected cases	Co-doped systems (TM+X where TM=V,Nb,Ta,Mo,W; X=N,C) energetically stable; Ta+N co-doping gives most significant band gap narrowing (1.09 eV); passivated co-doping eliminates mid-gap recombination centers
C-, Si-, N-, P-, S-, Se-, F-, Cl-, Br- and I-doped $BaTiO_3$ [88]	Hybrid DFT (HSE06), VASP	N doping most effective for band gap narrowing; C@O and I@O extend absorption to visible; S/Se improve photo-oxidation and photo-reduction

Zr+(S, Se and Te) codoped $BaTiO_3$ [89]	Full-potential linearized augmented plane-wave (FLAPW), $2 \times 2 \times 2$ supercell, $12 \times 12 \times 12$ k-mesh	Zr+X co-doping converts BTO to direct band gap; band edge positions favorable for overall water splitting; thermodynamic stability improved under both O-rich and O-poor conditions; photocatalytic performance of Zr+S and Zr+Se codoped $BaTiO_3$ are found to be better under visible light
Rh-doped $BaTiO_3$ [90–92]	DFT, VASP, Quantum ESPRESSO, LDA, norm-conserving pseudopotentials, 120 Ry cutoff, K-point mesh: $4 \times 4 \times 4$, $8 \times 8 \times 8$	Rh at Ba sites: Rh^{3+} donor states, narrowing of the band gap, 96% decomposition of methylene blue within 120 minutes; Rh at both sites introduces deleterious acceptor states; a strategy for selective doping has been demonstrated. Rh ions, by acquiring electron density from O, stabilise the intermediate oxidation state (3+/4+) during the oxidation of water. The surface of TiO_2-terminated BTO (001) is the most promising for catalysis. DFT confirms the role of Rh in modifying the electronic structure and shifting the position of the d-bands
Rh-doped $BaTiO_3$, bulk and (001) surface [93]	VASP, HSE06 and PBE+U (U = 2.6 eV on Ti 3d, 5.5 eV on Rh 4d), implicit solvent (VASPsol), nonadiabatic dynamics in the Redfield formalism	Rh at Ti sites of the (001) surface combines visible-light absorption, sub-picosecond non-radiative relaxation and efficient charge separation; in the bulk, Rh at Ti sites gives bright transitions at 2.19–2.64 eV. The Rh-doped (001) surface is proposed as a photoanode for photoelectrochemical water splitting

N-, F- and Rh-doped $BaTiO_3$ in contact with water [94]	Cluster DFT (Gaussian16, HSE screened hybrid, def2-TZVP basis) and ReaxFF molecular dynamics of a TiO_2-terminated (001) slab with water at 300 K	N and Rh substitution increases the covalent character of the Ti–N and Rh–O bonds, whereas F gives ionic Ti–F bonding. F substitution suppresses O–H bond formation at the surface and promotes ordered hydration layers near Ti sites
Ir-doped $BaTiO_3$ [95]	Experimental + DFT characterization	Ir^{3+}:BTO exhibits approximately a 1.6-fold increase in photocurrent under visible light; a 100-fold increase in H_2 evolution compared to Ir^{4+}:BTO; and improved charge transport dynamics as well as Faradaic efficiency
Cu-doped $BaTiO_3$ [96]	Experimental + DFT	Copper doping enhances photocatalytic activity for environmental remediation. This high efficiency is due to a narrower bandgap, a large surface area, and the suppression of charge carrier recombination
Anion–anion codoped $BaTiO_3$ [97]	Hybrid DFT (HSE06)	Anion–anion co-doping strategy for water splitting under visible light. Systems with double bonding (e.g., N–N, C–S, N–P) exhibit lower formation energies than their single-bonded counterparts, making them more thermodynamically favorable. N–N double bonding is the most stable due to similar atomic radii and strong anionic interactions

Pt-doped $BaTiO_3$ [98]	DFT, GGA-PW91, PAW, 300 eV cutoff, $4 \times 4 \times 4$ k-mesh, scissor operator 0.75 eV	Platinum doping in the barium and titanium sites (ratio of 0.125); strong Pt_{5d}/O_{2p} hybridization; introduction of ferromagnetism; mixed ionic–covalent character of the bonding
La-N codoped $BaTiO_3$ [99]	Materials Studio, GGA-PBE, GGA+U (U=4.3 eV Ti-3d, 8.1 eV La-4f), 500 eV cutoff, $3 \times 3 \times 3$ k-mesh	La@Ba reduces the bandgap to 1.55 eV; N@O reduces it to 1.23 eV; La-N@Ti (25%) creates midgap states, improves visible light absorption, and enhances water splitting efficiency
Ni-doped $BaTiO_3$ [100]	VASP, spin-polarized DFT, PAW, 520 eV cutoff, machine learning potential (MLP), metadynamics	Nickel doping lowers the energy barrier for the formation of O–O bonds; $\Delta G^{\ddagger}$ ($O^* \rightarrow O_2^*$): 1.57 eV (BTO), 1.20 eV (Ni/BTO); endothermic oxygen desorption: 1.37 eV (BTO), 0.97 eV (Ni/BTO)
TM(Transition Metal: V, Cr, Mo, Ta, Ru)-doped $BaTiO_3$ [101]	VASP 5.4.4, GGA-PBE, DFT-D3, 520 eV cutoff, $4 \times 4 \times 1$ k-mesh, MLP training on 16,162 configurations	Doping with transition metals increases the density of states at the Fermi level; effective polarization: $P_{\uparrow} > P_{\downarrow} > P$ (31.1, -4.1 and -39.2 μC cm^{-2}); the polarization state has a significant effect on surface reconstruction, but doping with transition metals does not alter the overall polarization trend
Cu-Te-codoped $BaTiO_3$ [102]	VASP, GGA-PBE, PAW, 550 eV cutoff, $6 \times 6 \times 6$ k-mesh, GGA+U (6 eV on Cu)	codoping with Cu and Te ($\sim$11%) reduces the bandgap width; the work function was calculated for BaO- and TiO_2-terminated slabs; calculations were performed taking spin polarization into account

$SrFeO_{3-\delta}$-doped $BaTiO_{3-\delta}$ [103]	DFT-based study combined with experiment	At a $SrFeO_{3-\delta}$ concentration of 5%((1-x)$BaTiO_{3-\delta}$-x$SrFeO_{3-\delta}$, x=0.05), the optical properties improved due to a narrowing of the bandgap. Magnetic measurements revealed an increase in ferromagnetic order. Dielectric measurements showed an increase in the dielectric constant
Sr-doped $BaTiO_3$ [104]	Wien2K package, DFT + experiment	Doping with strontium induces a phase transition from a tetragonal (ferroelectric) to a cubic (paraelectric) structure; the piezoelectric parameters (P_r, e_{33}, d_{33}) agree with experimental data; the bandgap narrows with increasing strontium content; potential for application in optoelectronics and solar cells
$SrTi_{1-x}Co_xO_{3-\delta}$ (x = 0, 0.125, 0.25, 0.375, and 0.5) [105]	GGA/GGA+U + experiment	Co doping enhances photocatalytic water splitting
Se/Mn codoped $SrTiO_3$ [106]	GGA with PBE	Se/Mn and Te/Mn codoping for visible-light H_2 production
Mo/P codoped $SrTiO_3$ [107]	GGA + U	Codoping with the metal Mo and the non-metal P can effectively narrow the bandgap and enhance the absorption of visible light. Furthermore, it has been established that the position of the band edges after co-doping (Mo + P) is thermodynamically favorable for water splitting
La/Al codoped $SrTiO_3$ [108]	Experimental (flux treatment after grinding) + DFT characterization	Al doping passivates trap states associated with oxygen vacancies; surface engineering effects are significant

Co-doped $SrTiO_3$ [109]	Experimental results (TRPL, TPV, UV–Vis DRS, ESR, etc.) and DFT calculations (GGA-PBE, B3LYP/6-31G*)	Co doping shifts the center of the $SrTiO_3$ d-band upwards, optimises the SO_4^- adsorption energy, broadens the response range to sunlight, and significantly increases the charge carrier extraction efficiency
Se/Zr codoped $ATiO_3$ [110]	GGA	The calculated formation energies for the co-doped systems range from -1.01 to -3.32 Ry/atom, confirming their thermodynamic stability. Analysis of the band-edge potentials shows that $CaTiO_3$ compounds co-doped with Se and Zr meet the necessary criteria for water photodissociation, which gives them the ability to generate H_2 and O_2 under the influence of light
Al-doped $SrTiO_3$ [111]	HSE06 hybrid functional	Al doping leads to the formation of $[V_O–Al_{Ti}]$ defect complexes. Substitution of Al for a Ti atom adjacent to an oxygen vacancy deactivates the $Ti_{3d}–Ti_{3d}$ interaction, eliminating intra-band states, as the key factor is the absence of valence d-orbitals in Al, which rationalizes the near-unity quantum efficiency of water splitting achieved experimentally [112]

S/Se/Te-doped $SrTiO_3$ [113]	Wien2k, GGA + TB-mBJ	The bandgap is 1.355 eV, 0.653 eV and 0.632 eV for $SrTiO_3$ doped with 12.5% S, Se and Te, respectively. For pure $SrTiO_3$, bandgap is 2.584 eV. At zero frequency, the dielectric constant ($\varepsilon_1(0)$) was 4.432 for pure $SrTiO_3$ and 6.332 for $SrTiO_3$ doped with Te (12.5%) in GGA-PBE, and ($\varepsilon_1(0)$) = 4.432 and 12.217 for GGA + mBJ. Optical conductivity of Te-doped $SrTiO_3$ was determined to be $0.322 \times 10^4\ \Omega^{-1}\,cm^{-1}$, compared with a value of $0.377 \times 10^4\ \Omega^{-1}\,cm^{-1}$ for mBJ
Ca/Zr-doped $BaTiO_3$ [114]	CASTEP, USP (ultra-soft pseudopotential)	When doped with Ca (BCTO), the Fermi level shifts towards the valence band, whilst the bandgap decreases from 1.726 eV to 1.714 eV. At the same time, upon doping with zirconium (BZTO) and Ca:Zr (BCZTO), a shift of the Fermi level towards the conduction band was observed, whilst the bandgap width increases to 1.776 eV and 2.654 eV, respectively

The doping of perovskite titanates $BaTiO_3$ and $SrTiO_3$ opens up broad possibilities for the targeted optimization of their properties, particularly in the context of photocatalysis. Summarizing the results of numerous studies, it can be stated that the introduction of both cationic and anionic dopants, especially in the form of co-doping, allows for the simultaneous solution of several key problems: significantly narrowing the bandgap, converting it to a direct bandgap, broadening absorption into the visible and near-IR regions, suppressing charge carrier recombination, and improving the positioning of the band edges relative to the reduction and oxidation levels of water. Note that the band gaps in Table 3 were obtained with different exchange–correlation functionals; their absolute values are therefore not directly comparable, and only the changes relative to the pristine material computed at the same level of theory should be compared.

These effects are most pronounced when transition metals and their combinations with nonmetals are used. For example, molybdenum doping, due to

bto.png bto.png

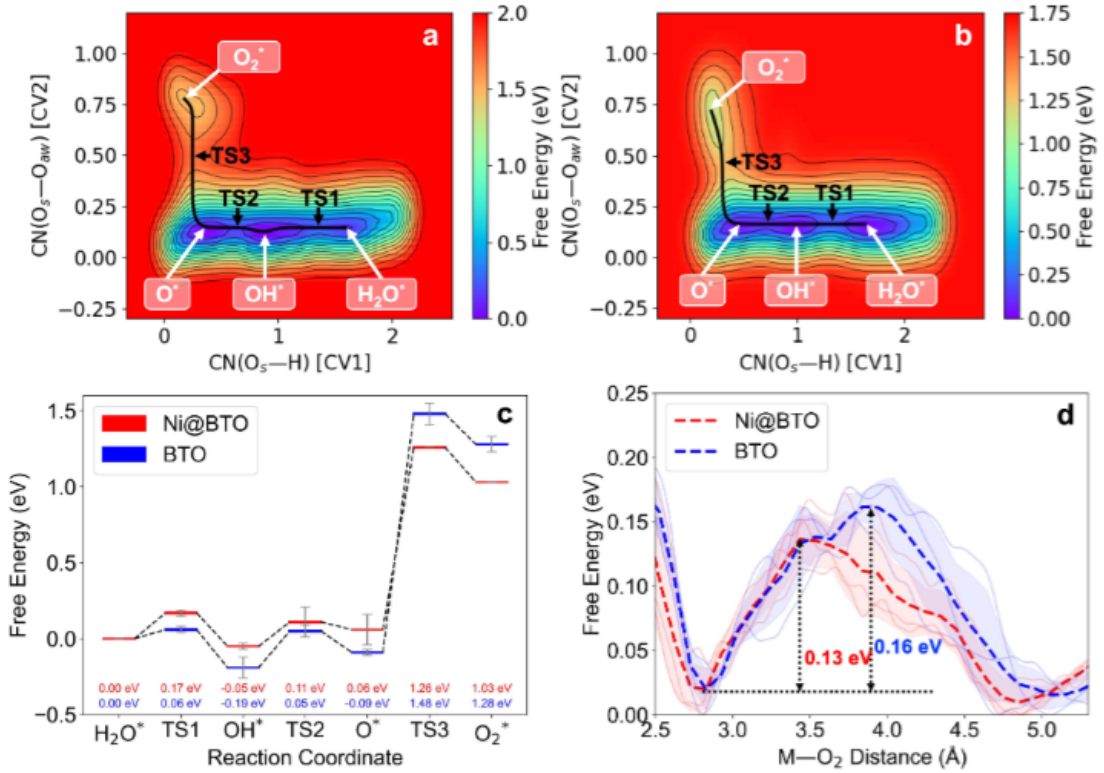

Figure 7. Free energy surface of OER on (a) BTO and (b) Ni@BTO from metadynamics. (c) Free energy profiles of OER on BTO (blue) and Ni@BTO (red). (d) Free energy profiles of O_2 desorption [100].

strong $Ti_{3d}-Mo_{4d}$ hybridization, reduces the bandgap to 1.27 eV and nearly doubles the hydrogen evolution rate (up to 63 mmol g^{-1} h^{-1}). Rhodium in the barium position (Rh^{3+}) not only narrows the bandgap and introduces donor states, but also stabilizes intermediate oxidation states, ensuring 96% decomposition of methylene blue within 120 minutes; the corresponding changes in the density of states of Rh-doped $BaTiO_3$ surfaces are shown in Figure 8 [91]. Nonadiabatic dynamics further shows that Rh at Ti sites of the (001) surface combines visible-light absorption with fast charge separation, which makes this surface a candidate photoanode [93]. Iridium in the Ir^{3+} state yields a 1.6-fold increase in photocurrent and a 100-fold increase in the rate of H_2 production compared to Ir^{4+}, significantly improving charge transport. Nickel effectively lowers the energy barriers for oxygen formation and desorption, which is critical for the O_2 evolution reaction (Figure 7).

Co-doping exhibits a synergistic effect. The Ta+N combination yields the largest band gap narrowing (1.09 eV) among the studied pairs, and passivated co-doping eliminates mid-gap recombination centers [87]. The Zr+S, Zr+Se, and Mo/P pairs provide a thermodynamically optimal arrangement of band edges for complete water splitting under visible light. La–N co-doping forms mid-gap states, sharply enhancing visible light absorption and the efficiency of photocatalytic water splitting. In $SrTiO_3$, aluminum, by forming [V_O-Al_{Ti}] complexes, almost completely suppresses intraband states, consistent with the near-unity quantum efficiency of water splitting achieved experimentally [111,

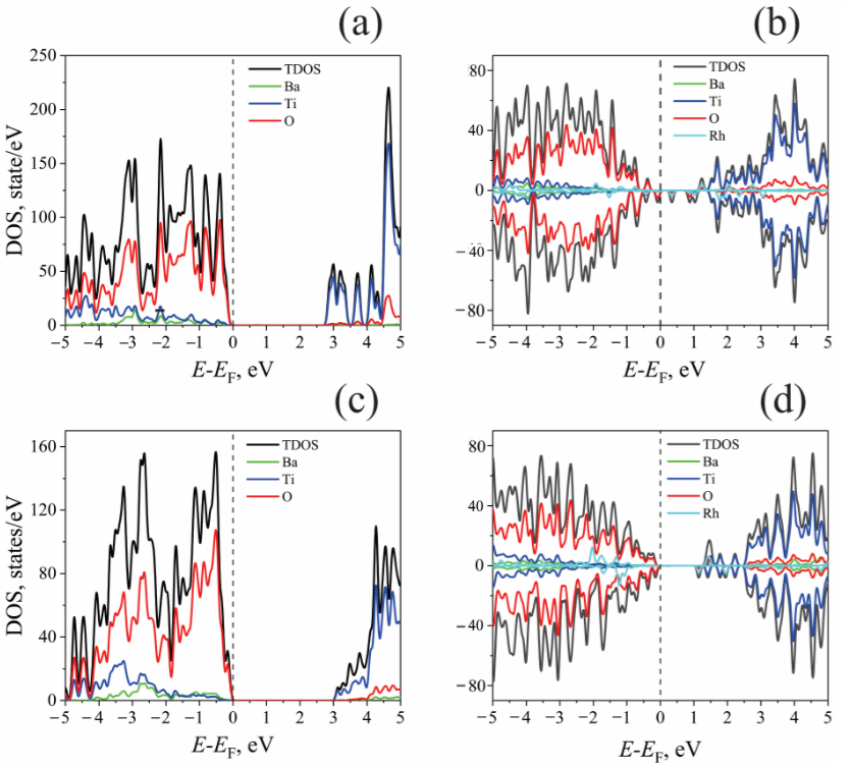

Figure 8. Total and partial DOS for undoped and Rh-doped TiO_2 - and BaO-terminated surfaces [91].

112].

Some co-doped systems, such as Zr+X-codoped $BaTiO_3$ [89], not only improve optical and electronic properties but also show enhanced thermodynamic stability under both O-rich and O-poor conditions. The dopant also changes the interaction of the surface with water: F substitution suppresses O–H bond formation and promotes ordered hydration layers, whereas N and Rh increase the covalency of the metal–ligand bonds [94]. At the same time, doping often affects the phase composition (for example, Sr transforms $BaTiO_3$ from a ferroelectric tetragonal phase to a paraelectric cubic phase), optical constants, and even magnetic properties, which opens up additional opportunities for creating multifunctional photocatalysts.

Thus, the doping strategy allows one to overcome the fundamental limitations of pure $BaTiO_3$ and $SrTiO_3$—a wide bandgap and low visible-light utilization efficiency—and transform these readily available perovskites into highly active materials for visible-light photocatalysis. The obtained data provide a solid foundation for the development of efficient systems for hydrogen production, the degradation of organic pollutants, and other processes with environmental and energy applications, making titanates a promising platform for practical use in solar energy and environmental protection.

3.3 Computation of heterostructures

The next, more complex stage in the modification of perovskite materials involves the creation of heterostructures. Combining perovskite with other semiconductors, metals, or carbon-based materials allows not only for the adjustment of

the bandgap width but also for the formation of favorable band alignments that facilitate charge transport across the interface. Such heterostructures often exhibit significantly higher photocatalytic activity and stability compared to individual components. Table 4 summarizes published calculations of perovskite-based heterostructures. For each system, it lists the computational method and the main reported results on the interface electronic structure and, where available, the photocatalytic performance.

Table 4. Calculations of perovskite-based heterostructures.

System	Methods	Main results
SRO/BTO/mSTO/SRO (m=0, 2, 4 u.c.) [115]	DFT+NEGF (SIESTA 4.1.5), GGA-PBE, DFT+U on Ti_{3d} and O_{2p}, Troullier-Martins pseudopotentials, 150–250 Ry cutoffs	The band alignment diagrams show polarisation-dependent Schottky/ Ohmic contacts; for m(STO)=2, TER $\sim 10^4$% and TMR $\sim 10^5$%; the DFT+U band gap of the bulk material is close to experiment but is significantly reduced in the layered structures; the interfacial magnetoelectric coupling is weak or moderate
$BaTiO_3/SrTiO_3$(001) [116]	Hybrid DFT (B3PW)	Bandgap width in bulk BTO: 3.55 eV; STO: 3.96 eV; combined lattice constant: 3.958 Å; band edge shifts depending on the termination; surface energy of TiO_2-terminated BTO (001): 1.07 eV per surface unit cell; BaO-terminated: 1.19 eV per surface unit cell; all heterostructures remain semiconducting
$BaTiO_3$/n-$SrTiO_3$ [117]	Quantum ESPRESSO, LDA, LDA+U, HSE hybrid functional, Ultrasoft pseudopotentials, 40 Ry cutoff, $6 \times 6 \times 1$ k-mesh	HSE results in a CBM shift of just 0.03 eV between BTO and STO; polarisation switching stimulates interfacial metallisation; the operating mechanism of an active ferroelectric field-effect transistor has been demonstrated

$BaTiO_3/SrTiO_3$ [10]	VASP, GGA-PBE+U (U = 4.0 eV on Ti), DFT-D3, 520 eV cutoff, $5 \times 5 \times 1$ k-mesh, external field 0.1 eV/Å along [001]	Bandgap width of the BTO/STO heterojunction: 1.1 eV (compared to 2.31 eV for STO and 2.15 eV for BTO); under the influence of an external field, it narrows to 1.0 eV; $\Delta G_H^* = -0.42$ eV; electron transport from BTO to STO; the piezoelectric field reduces the bandgap width of the heterojunction nanofibres; H_2 evolution rate: 1950.2 μmol g^{-1} h^{-1} under light and ultrasound, about 2.3 and 4.1 times higher than for pristine STO and BTO under light alone
$BaTiO_3/SrTiO_3$ [118]	DFT+NEGF	In asymmetric tunnel junctions, TMR and TER coexist. The value depends on the thickness of the STO dielectric layer
$PbTiO_3/SrTiO_3$ [119]	LDA (PWSCF), Vanderbilt ultrasoft pseudopotentials, 30 Ry cutoff, $6 \times 6 \times 3$ k-mesh, Berry-phase polarization	Strong Pb-O and Ti-O hybridisation; mismatch strain and the internal electric field polarise the ST layers; PST behaves as a single artificial ferroelectric material at short modulation lengths; polarisation decreases with increasing STO volume fraction
Sub-nm PtO_x on oxygen-deficient $BaTiO_3$ [120]	VASP, GGA-PBE, PAW, 520 eV cutoff, $2 \times 2 \times 1$ k-mesh	Pt-O-Ti^{3+} charge separation sites; H_2 generation: 1891 μmol g^{-1} h^{-1}; oxygen vacancies facilitate charge aggregation; Ti^{3+} defects enhance rapid electron transfer

$BaTiO_3/Cu_2O$ nanostructured heterojunction [121]	Quantum ESPRESSO, GGA-PBE, ultrasoft pseudopotentials, 30 Ry cutoff	Alignment of type II at the $BaTiO_3/Cu_2O$ interface; built-in dipole due to charge transport; lower effective electron mass in Cu_2O; photocurrent: 1.44 $mA\,cm^{-2}$ at 0.95 V; conversion efficiency: 0.66%
$BaTiO_3/LaAlO_3$ heterostructure [122]	Quantum ESPRESSO, GGA-PBE, norm-conserving pseudopotentials, $10 \times 10 \times 1$ k-mesh, 45 Ry cutoff, DFT-D3(BJ)	Crystal lattice mismatch of -3.16%. The BTO(001) surface gives the lowest band gap (3.44 eV), whereas BTO(011) and (111) show direct band gaps of 4.05 and 3.75 eV, respectively. Dynamic and thermal stability confirmed at 300 K using ab initio MD
$CaSnO_3/SrTiO_3$ and $ZnSnO_3/SrTiO_3$ [123]	VASP, GGA-PBE, cutoff energy 450 eV, $4 \times 4 \times 1$ k-points	modeled $(CSO)_n/(STO)_4$ and $(ZSO)_n/(STO)_4$ (n = 1, 3, 5, 7, 10). The bandgap narrowed to 0.502 eV for CSO/STO and 0.349 eV ZSO/STO compared to the pure bulk material STO, where this value reaches 1.802 eV. The effective electron masses were also calculated, these were significantly smaller than those of the pure sample, specifically (0.31 and 0.40 m_0) and (0.38 and 0.52 m_0) for $(CSO)_7/(STO)_4$ and $(ZSO)_1/(STO)_4$ compared to bulk STO (7.03 and 0.94 m_0) along the $\Gamma - X$ and $\Gamma - M$ directions

$LaInO_3/BaSnO_3$ heterostructure with $BaTiO_3$ ferroelectric film [124]	VASP, PAW pseudopotentials, GGA-PBE, cutoff energy 400 eV, $4 \times 4 \times 1$	Depositing a $BaTiO_3$ film onto the surface of a $LaInO_3/BaSnO_3$ heterostructure can significantly increase the electron density at the heterostructure interface. The direction and intensity of the ferroelectric polarization of the top $BaTiO_3$ film play an important role in optimizing the electronic properties of the $LaInO_3/BaSnO_3$ interface

In the paper [115], calculations using DFT methods with spin polarisation for the SRO/BTO/mSTO/SRO structure (where $m = 0, 2, 4$ unit cells; Figure 9) show that the direction of the ferroelectric polarisation in barium titanate determines the nature of the band alignment. Specifically, for $m = 0$, either Schottky barriers or ohmic contacts form at the interfaces, whereas for $m = 2$ and 4, only Schottky contacts form. It has been established that under P-polarisation, the charge flowing out of the metallic $SrRuO_3$ shifts the $SrTiO_3$ conduction band minimum by ~ 1.5 eV, thereby creating triangular barriers corresponding to Fowler–Nordheim tunnelling. The authors note that the heterostructure with $m = 2$ exhibits the strongest magnetoelectric response with giant tunnel electrical resistance (TER up to 10^4 %) and tunnel magnetoresistance (TMR up to 10^5 %) at 0 K, although the interfacial coupling remains insufficient to switch the TMR solely by changing the polarity. Although this work focuses on a description at the GGA level, which captures the main mechanisms of charge transport and polarisation screening at oxide interfaces, the neglect of defects and the assumption of ballistic transport point to key directions for future multiscale modelling of real ferroelectric tunnelling junctions consisting exclusively of oxides.

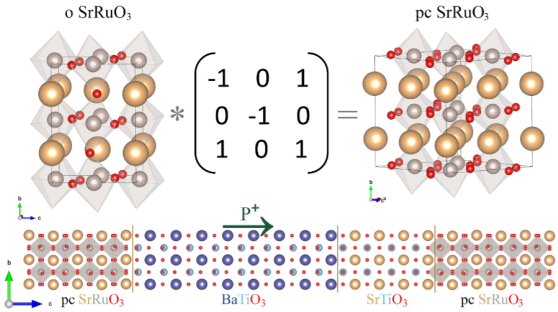

Figure 9. Slab model of the SRO/BTO/4STO/SRO junction [115].

As part of the study [116], using a hybrid DFT method, Eglitis and his colleagues carried out systematic calculations using the CRYSTAL code and B3LYP/B3PW functionals for the $BaTiO_3/SrTiO_3$ (001) heterointerface, modelled

as a single slab with BO_2 or AO termination (Figure 10). The electronic structure, in particular the $\Gamma-\Gamma$ gap and the Mulliken charge distribution at the interface, was evaluated alongside atomic deformation and relaxation. This allowed clear systematic trends to be identified in perovskite-based heterostructures. In contrast to the GGA+U study discussed above [115], a hybrid approach accounting for exchange and correlation significantly improves the description of electronic states at the interface compared to standard GGA approaches, whilst the isolated-slab model highlights intrinsic interface effects without periodic boundary artefacts in the third dimension.

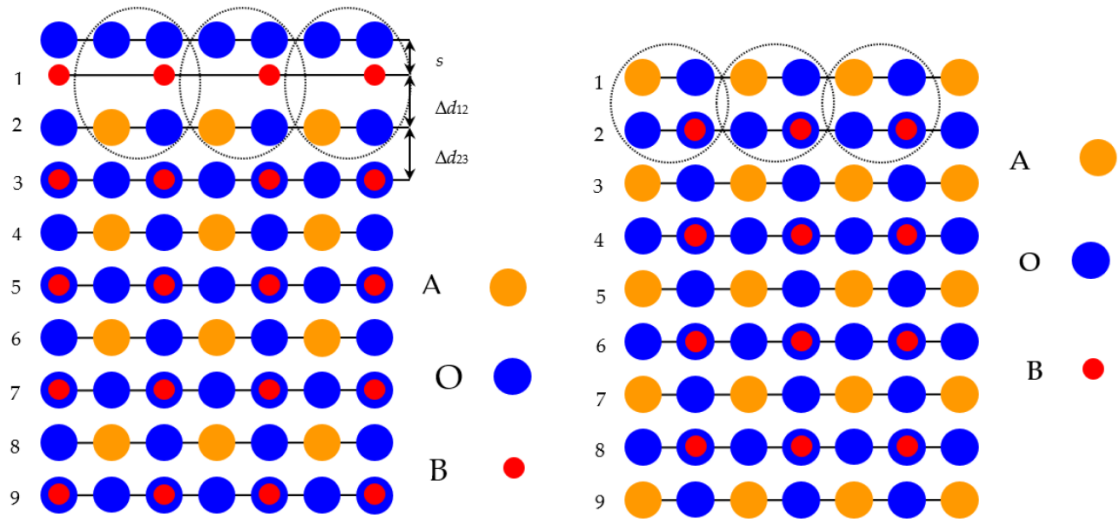

(a) BO_2 -terminated (b) AO-terminated

Figure 10. (001) surface of ABO_3 perovskite with (a) BO_2 and (b) AO termination [116].

Although this study provides valuable insights into how interface formation alters the bandgap width and local bonds compared to the bulk material, it does not investigate polarisation screening, charge transport beyond the Mulliken analysis, or implications for functional devices such as photocatalysis or dielectric response. The results of this study highlight the exceptional utility of hybrid functionals for accurately determining trends in the electronic structure of oxide-based heteroepitaxial systems and lay the groundwork for future simulations incorporating defects or dynamic simulations.

Liu et al. [117] performed first-principles DFT calculations (Quantum ESPRESSO, LDA/LDA+U) for $BaTiO_3$/n-$SrTiO_3$ heterostructures to demonstrate polarisation-induced doping modulation, whereby a change in the direction of the ferroelectric polarisation in $BaTiO_3$ causes significant electron transport across the interface with TiO_2. When the polarisation is directed into the n-$SrTiO_3$ layer, the conduction band minimum of the two boundary $BaTiO_3$ unit cells drops below the Fermi level, leading to the metallisation of these layers and the formation of a 2DEG with an excess carrier density of ~ 0.12 electrons per unit cell. Opposite polarisation depletes the carriers, rendering the interface insulating. An extended electrostatic model, incorporating Thomas–Fermi screening, quantitatively accounts for the spatial distribution of the transferred charge and a band gap shift of ~ 1.7 eV between the polarisation states, whilst the conduction band offset between $BaTiO_3$ and $SrTiO_3$ lies in the range of 0.03–0.2 eV depending on the

functional. It is shown that the same mechanism operates in $PbTiO_3/n\text{-}SrTiO_3$, suggesting broad applicability for the design of active ferroelectric field-effect transistors. Although the calculations reflect the fundamental physics of charge transport and interface metallisation, the use of LDA (with post-hoc corrections) and idealised defect-free slabs leaves open questions regarding realistic doping profiles, scattering mechanisms and high-frequency dielectric response in functional devices.

Caffrey et al. [118] performed first-principles calculations of electron transport (SIESTA+SMEAGOL) using the NEGF method to demonstrate the coexistence of giant tunnelling resistance and magnetoresistance in an all-oxide magnetic tunnel junction $SrRuO_3/BaTiO_3/mSrTiO_3/SrRuO_3$. The insertion of a thin $SrTiO_3$ layer at one of the interfaces allows the composite barrier profile to be modulated under the control of polarisation via rigid potential shifts and depolarisation charge transport, leading to TER coefficients that grow exponentially with the thickness of $SrTiO_3$ (up to 212.84 at $m = 2$), whilst the TMR (exceeding 10) remains stable due to the identical symmetry of the $BaTiO_3$ and $SrTiO_3$ complex bands. The ferroelectric polarisation of $BaTiO_3$ (35.5 $\mu\,C\,cm^{-2}$ under epitaxial strain) determines the tunneling conductivity without compromising the spin-filtering efficiency of the $BaTiO_3$ barrier, creating four well-separated resistive states suitable for multi-state memory. Although the LSDA+ASIC description and the ideal interface model reflect the fundamental physical processes of polarisation screening and band alignment at the $BaTiO_3/SrTiO_3$ interface, the neglect of defects and phonon scattering leaves questions regarding the actual device characteristics unresolved.

Guo and his colleagues [10] performed first-principles DFT calculations (VASP, PBE+U with U = 4.0 eV on Ti and DFT-D3 dispersion correction) for a $SrTiO_3/BaTiO_3$ bilayer heterostructure in order to elucidate the electronic reasons behind its excellent piezo-photocatalytic properties. The interface forms a Z-scheme heterojunction with a significantly reduced bandgap (1.1 eV) compared to the parent perovskites (2.31 eV for STO, 2.15 eV for BTO), which narrows further to 1.0 eV under the influence of an external electric field of 0.1 eV/Å, simulating the piezotronic effect and selectively shifting the conduction band minimum. Differential charge density maps confirm the directional transport of electrons from $BaTiO_3$ to $SrTiO_3$, creating an intrinsic field that promotes carrier separation via the Z scheme, whilst the calculated free hydrogen adsorption energy of -0.42 eV at the heterojunction optimises HER kinetics. These modifications to the electronic structure (bandgap engineering, charge redistribution at the phase boundary, and field-induced band bending) directly underpin the experimentally observed red shift in optical absorption and the hydrogen evolution rate of 1950.2 $\mu\,mol\,g^{-1}\,h^{-1}$ under combined light and ultrasonic excitation, which is about 2.3 and 4.1 times higher than the photocatalytic rates of pristine $SrTiO_3$ and $BaTiO_3$ measured under light alone, and exceeds the values previously reported for perovskite-based piezo-photocatalysts, highlighting the synergy between ferroelectric polarisation and the dynamics of the photocatalytic charge at the $BaTiO_3/SrTiO_3$ interface.

Among the computational approaches examined in this sample of studies,

hybrid functionals such as B3LYP/B3PW and HSE06 demonstrate the strongest physical justification. In the screened hybrid HSE06 functional, used in several of the reviewed works [80, 82, 88, 93, 97, 111, 117], a quarter of the short-range semilocal exchange is replaced by exact Hartree–Fock exchange [125]:

$$E_{xc}^{\mathrm{HSE06}} = \tfrac{1}{4}E_x^{\mathrm{HF,SR}}(\omega) + \tfrac{3}{4}E_x^{\mathrm{PBE,SR}}(\omega) + E_x^{\mathrm{PBE,LR}}(\omega) + E_c^{\mathrm{PBE}}, \qquad (1)$$

where SR and LR denote the short- and long-range parts of the Coulomb interaction, separated by the screening parameter $\omega = 0.2\ \text{Å}^{-1}$. The practical use of hybrid functionals is nevertheless constrained by substantial computational cost, which becomes prohibitive for systems containing a large number of atoms. For this reason, finite-temperature and environmental effects are usually treated with less expensive methods: molecular dynamics is performed at the DFT+U level and combined with static hybrid calculations [82, 93], reactive force fields describe the interaction of the surface with water [94], and DFT calculations of molecular structure are combined with classical all-atom molecular dynamics to describe ion transport, as in proton exchange membranes of hydrogen fuel cells [126]. By contrast, the DFT+U approach offers a more computationally tractable alternative capable of yielding reasonably accurate results; when the U parameter is carefully chosen for the Ti_{3d} and O_{2p} states, this method can approach the accuracy achieved by hybrid functionals. The GGA-PBE and LDA functionals, despite being widely employed, fail to reproduce accurate band gap values, which restricts their reliability for calculating electronic properties. The choice of functional is therefore a critical consideration in the design of computational studies of perovskite heterostructures, particularly when the goal is to predict photocatalytic performance.

4. Photocatalytic performance of BTO/STO heterostructures

Compared with the large number of studies on BTO/STO films and superlattices for dielectric and ferroelectric applications (Table 1), experimental studies of BTO/STO heterostructures for photocatalysis remain scarce. The available works have used nanostructured powders rather than epitaxial films: nanofibers [9, 10], core–shell nanowires [11] and nanocomposites [127]. In these works, illumination is combined with mechanical (usually ultrasonic) excitation, so that the piezoelectric response of $BaTiO_3$ adds to the built-in field at the interface. The reported conditions and performance are summarized in Table 5.

Guo et al. [10] prepared STO/BTO nanofibers by electrospinning and tested them with 1 wt.% Pt as a co-catalyst and methanol as a hole scavenger. Under combined light and ultrasound, the heterojunction produced 1950.2 $\mu\,\text{mol}\,\text{g}^{-1}\,\text{h}^{-1}$ of H_2, whereas a physical mixture of the two oxides gave 824.7 $\mu\,\text{mol}\,\text{g}^{-1}\,\text{h}^{-1}$ under the same excitation. This comparison indicates that the enhancement originates from the interface rather than from the presence of both phases. The activity decreased by about 20% over five 3-h cycles and was restored by adding methanol, which the authors attributed to consumption of the sacrificial

Table 5. Experimental photocatalytic performance of BTO/STO heterostructures.

Catalyst	Preparation	Test conditions	Performance	Ref.
STO/BTO nanofibers	Electrospinning, calcination at 750 °C	H_2 evolution; 300 W Xe lamp + ultrasound (40 kHz, 90 W); 1 wt.% Pt; 10 vol.% methanol	1950.2 μmol g^{-1} h^{-1} (light + ultrasound), 2.3 and 4.1 times the light-only rates of pure STO and BTO; physical mixture: 824.7 μmol g^{-1} h^{-1}; $\sim$20% loss over 5 cycles	[10]
BTO@STO core–shell nanowires, Sr:Ba = 2.5:7.5–7.5:2.5	–	H_2 evolution; light + ultrasound	18.0 μmol g^{-1} min^{-1} (Sr:Ba = 7.5:2.5) vs 7.0 (BTO) and 6.0 (STO)	[11]

agent. Mohan et al. [11] observed a similar trend for $BaTiO_3$@$SrTiO_3$ core–shell nanowires: the H_2 evolution rate increased from 7.0 ($BaTiO_3$) and 6.0 ($SrTiO_3$) to 18.0 μ mol g^{-1} min^{-1} for the sample with the highest Sr content.

These results indicate that BTO/STO heterostructures outperform the individual oxides, particularly when light is combined with ultrasound. However, the activities were measured with different co-catalysts, sacrificial agents, light sources and ultrasonic powers, and are normalized per unit mass; apparent quantum yields are rarely reported. In addition, the contribution of cavitation-induced sonochemical reactions has to be separated from the piezoelectric effect by control experiments. Standardized metrics are therefore needed before the different BTO/STO architectures can be compared quantitatively. Together with the small number of available studies, this shows that photocatalytic testing of well-defined BTO/STO interfaces, including epitaxial heterostructures prepared by the methods listed in Table 1, remains an open research direction.

5. Conclusion

In this review, we have systematically examined the electronic and structural properties of perovskite oxides for advanced photocatalytic applications, progressing from pristine structures and native defects to doping strategies and, ultimately, to high-performance heterostructures.

Section “Computation of single systems” traces the development of methodological frameworks employed in perovskite research, spanning from conventional GGA-PBE and LDA approaches to more advanced treatments, including the hybrid HSE06 functional, DFT+U+V with self-consistent parameter calibration, and neural network potentials trained on DFT data, which enable the simulation of both static configurations and vacancy dynamics. Particular attention should be paid to the study by Choi et al. [79], which offers a methodological caution:

the application of DFT+U without self-consistent parameter calibration may introduce inaccuracies in band gap estimates and band edge positions, both of which are essential for photocatalytic performance. The same study demonstrates that self-consistent calibration of the U and V parameters yields accuracy comparable to that of hybrid functionals while incurring substantially lower computational costs. Collectively, the reviewed investigations indicate that oxygen vacancies are an important means of tuning the electronic properties of perovskites, even in the absence of extrinsic doping. Furthermore, considerable variation in computed band gaps and band edge positions is observed depending on the chosen functional, underscoring the necessity of careful method selection to ensure reliable predictions of photocatalytic behavior.

With respect to doping, the analysis presented in Section "Computation of doped systems" indicates that co-doping often yields stronger band gap narrowing and fewer mid-gap recombination centres than single-element doping. The combination of anionic and cationic dopants tends to produce more pronounced effects than either dopant type in isolation, both for $BaTiO_3$ and $SrTiO_3$ hosts; however, these results were obtained with different functionals and models and are not directly comparable. Particular attention should be paid to the study by Chandrappa et al. [95], which demonstrates that Ir doping in the Ir^{3+} oxidation state results in a 1.6-fold enhancement of the photocurrent and a 100-fold increase in the H_2 evolution rate compared to Ir^{4+}, thereby substantially facilitating charge transfer processes.

The findings discussed in Section "Computation of heterostructures" suggest that heterostructure formation is among the most effective strategies considered here. However, the reported enhancements cannot be ranked directly, because they refer to different baselines and experimental conditions: Ir doping in the Ir^{3+} state increases the H_2 evolution rate about 100-fold relative to Ir^{4+}-doped $BaTiO_3$ [95], whereas the $SrTiO_3/BaTiO_3$ nanofiber heterojunction reaches 1950.2 μmol g^{-1} h^{-1}, which is about 4.1 and 2.3 times higher than the light-only rates of pristine $BaTiO_3$ and $SrTiO_3$, respectively [10]. A reliable ranking of modification strategies would require comparable metrics, such as the apparent quantum yield measured under identical conditions. The experimental studies summarized in Table 5 confirm that BTO/STO heterostructures outperform the individual oxides, particularly under combined light and ultrasonic excitation, although such studies are still few.

Taken together, the reviewed results open promising avenues for the rational design of visible-light-active photocatalytic systems based on $BaTiO_3/SrTiO_3$ architectures. By further optimizing interface orientation, polarization direction, surface termination, and combining them with targeted doping or co-catalysts, further improvements in solar-to-hydrogen efficiency and CO_2 conversion may be achieved. We believe that carefully engineered $BaTiO_3/SrTiO_3$-based heterostructures can play a significant role in overcoming current limitations of photocatalytic technologies and accelerating the development of efficient, stable, and scalable solar-fuel production. Future efforts integrating theoretical modelling with experimental validation are needed to bring these materials closer to practical implementation in green hydrogen production and carbon-neutral

energy technologies.

Acknowledgement

This research was funded by the Science Committee of the Ministry of Science and Higher Education of the Republic of Kazakhstan "Development of hybrid perovskite nanostructures for hydrogen photogeneration" (Grant No. AP23489103).

References

[1] K. Villa et al., Sustainable Energy & Fuels **5** (2021) 4560–4569. [*CrossRef*]
[2] A. Kudo, Y. Miseki, Chemical Society Reviews **38** (2009) 253–278. [*CrossRef*]
[3] R. Li et al., Renewable and Sustainable Energy Reviews **206** (2024) 114863. [*CrossRef*]
[4] H. Nishiyama et al., Nature **598** (2021) 304–307. [*CrossRef*]
[5] P. Zhou et al., Nature **613** (2023) 66–70. [*CrossRef*]
[6] D. Zheng et al., Journal of Cleaner Production **414** (2023) 137700. [*CrossRef*]
[7] International Energy Agency, World Energy Outlook 2025 (IEA: Paris, 2025). [*Web Link*]
[8] J. Gao et al., Advanced Science **12** (2025) e08062. [*CrossRef*]
[9] X. Liu et al., Nano Energy **89** (2021) 106391. [*CrossRef*]
[10] M. Guo et al., Nano Energy **127** (2024) 109745. [*CrossRef*]
[11] H. Mohan, S. Vadivel, T. Shin, Ultrasonics Sonochemistry **101** (2023) 106650. [*CrossRef*]
[12] A.U. Abuova et al., Ceramics **8** (2025) 100. [*CrossRef*]
[13] R.I. Eglitis et al., Crystals **13** (2023) 799. [*CrossRef*]
[14] O. Abdirashev et al., International Journal of Molecular Sciences **27** (2026) 7975. [*CrossRef*]
[15] H. Tabata, H. Tanaka, T. Kawai, Applied Physics Letters **65** (1994) 1970–1972. [*CrossRef*]
[16] C. Merckling et al., Journal of Vacuum Science & Technology A: Vacuum, Surfaces, and Films **37** (2019) 021510. [*CrossRef*]
[17] J. Zhu et al., Ceramics International **34** (2008) 967–970. [*CrossRef*]
[18] M. Jimi et al., Thin Solid Films **486** (2005) 158–161. [*CrossRef*]
[19] L. Kim et al., Applied Physics Letters **87** (2005) 052903. [*CrossRef*]
[20] V. Gartnerova et al., Materials Research Bulletin **89** (2017) 180–184. [*CrossRef*]
[21] I. Olaniyan et al., ACS Nano **19** (2025) 37534–37543. [*CrossRef*]
[22] K.-G. Lim, K.-H. Chew, Integrated Ferroelectrics **223** (2021) 94–103. [*CrossRef*]
[23] M. Rioult et al., Applied Physics Letters **107** (2015) 103901. [*CrossRef*]
[24] A. Ohtomo, H.Y. Hwang, Nature **427** (2004) 423–426. [*CrossRef*]
[25] K.D. Fredrickson, A.A. Demkov, Physical Review B **91** (2015) 115126. [*CrossRef*]
[26] Q. Wu et al., Physical Review B **94** (2016) 155420. [*CrossRef*]
[27] J. Zhou et al., Physical Review B **93** (2016) 155167. [*CrossRef*]
[28] S.R. Lee et al., Nano Letters **19** (2019) 2243–2250. [*CrossRef*]

[29] W. Li, L. Gao, A.A. Demkov, Physical Review B **102** (2020) 035308. [*CrossRef*]
[30] I.I. Piyanzina et al., Ferroelectrics **542** (2019) 7–12. [*CrossRef*]
[31] S.N. Rebec et al., Proceedings of the National Academy of Sciences **116** (2019) 16687–16691. [*CrossRef*]
[32] P. Lutz et al., Physical Review Materials **2** (2018) 094411. [*CrossRef*]
[33] T.M. Shaw et al., Journal of Materials Research **9** (1994) 2566–2573. [*CrossRef*]
[34] B.D. Qu et al., Applied Physics Letters **72** (1998) 1394–1396. [*CrossRef*]
[35] A. Visinoiu et al., Applied Physics A **80** (2005) 229–235. [*CrossRef*]
[36] E. Lupi et al., Advanced Materials **35** (2023) 2302012. [*CrossRef*]
[37] G. Koebernik et al., Thin Solid Films **449** (2004) 80–85. [*CrossRef*]
[38] Y.J. Shin et al., ACS Applied Materials & Interfaces **9** (2017) 27305–27312. [*CrossRef*]
[39] H. Shigetani et al., Materials Science and Engineering: B **41** (1996) 148–151. [*CrossRef*]
[40] R.A. McKee et al., MRS Online Proceedings Library **341** (1994) 309. [*CrossRef*]
[41] A. Soukiassian et al., Journal of Materials Research **23** (2008) 1417–1432. [*CrossRef*]
[42] A.K. Manjeshwar et al., Nano Letters **25** (2025) 14246–14255. [*CrossRef*]
[43] S. Choo et al., Nano Letters **25** (2025) 17467–17474. [*CrossRef*]
[44] F. Niu, B.W. Wessels, Journal of Vacuum Science & Technology B: Microelectronics and Nanometer Structures Processing, Measurement, and Phenomena **25** (2007) 1053–1057. [*CrossRef*]
[45] A. Barbier et al., Journal of Applied Physics **112** (2012) 114116. [*CrossRef*]
[46] L. Mazet et al., Science and Technology of Advanced Materials **16** (2015) 036005. [*CrossRef*]
[47] W. Nunn et al., Journal of Vacuum Science & Technology A: Vacuum, Surfaces, and Films **39** (2021) 040404. [*CrossRef*]
[48] K. Fujimoto, Y. Kobayashi, K. Kubota, Thin Solid Films **169** (1989) 249–256. [*CrossRef*]
[49] T. Yasumoto et al., Japanese Journal of Applied Physics **39** (2000) 5369. [*CrossRef*]
[50] A.B. Posadas et al., ACS Applied Materials & Interfaces **13** (2021) 51230–51244. [*CrossRef*]
[51] E.J. Cukauskas et al., Applied Physics Letters **74** (1999) 4034–4036. [*CrossRef*]
[52] W. Zhang et al., Science and Technology of Advanced Materials **13** (2012) 035006. [*CrossRef*]
[53] F.A. Vargas et al., Thin Solid Films **596** (2015) 77–82. [*CrossRef*]
[54] M.S.I. Sumon et al., Journal of Physics: Materials **8** (2025) 045011. [*CrossRef*]
[55] S.Y. Jung et al., Journal of Advanced Ceramics **13** (2024) 1919–1930. [*CrossRef*]
[56] J. Lindner et al., MRS Proceedings **541** (1998) 501. [*CrossRef*]
[57] J. Lindner et al., Le Journal de Physique IV **9** (1999) Pr8-411–Pr8-418. [*CrossRef*]
[58] J. Lindner et al., Integrated Ferroelectrics **30** (2000) 53–59. [*CrossRef*]
[59] R. Pantou et al., Le Journal de Physique IV **11** (2001) Pr11-313–Pr11-317. [*CrossRef*]
[60] R. Xu et al., Thin Solid Films **406** (2002) 113–117. [*CrossRef*]

[61] T. Hosokura et al., Crystal Growth & Design **11** (2011) 4253–4256. [*CrossRef*]
[62] T. Hosokura et al., International Journal of Applied Ceramic Technology **9** (2012) 74–82. [*CrossRef*]
[63] A. Ramezani, H. Abdizadeh, M.R. Golobostanfard, Ceramics International **47** (2021) 17895–17906. [*CrossRef*]
[64] K. Bakken et al., Journal of Sol-Gel Science and Technology **95** (2020) 562–572. [*CrossRef*]
[65] T.Q. Ngo et al., Applied Physics Letters **104** (2014) 082910. [*CrossRef*]
[66] M. Vehkamäki et al., Electrochemical and Solid-State Letters **2** (1999) 504–506. [*CrossRef*]
[67] M. Falmbigl et al., The Journal of Physical Chemistry C **121** (2017) 16911–16920. [*CrossRef*]
[68] J.H. Shim et al., Journal of Materials Chemistry C **5** (2017) 8000–8013. [*CrossRef*]
[69] B.M. Coffey et al., Chemistry of Materials **31** (2019) 5558–5565. [*CrossRef*]
[70] A.V. Plokhikh et al., Journal of Materials Chemistry C **9** (2021) 13115–13122. [*CrossRef*]
[71] H.-Y. Choi et al., Materials Science in Semiconductor Processing **160** (2023) 107442. [*CrossRef*]
[72] B. Jalan et al., Journal of Vacuum Science & Technology A: Vacuum, Surfaces, and Films **27** (2009) 461–464. [*CrossRef*]
[73] H. Xu et al., Powder Technology **444** (2024) 119955. [*CrossRef*]
[74] W. Cai et al., Applied Surface Science **619** (2023) 156773. [*CrossRef*]
[75] H. Qiu et al., Journal of Materials Chemistry A **11** (2023) 7034–7042. [*CrossRef*]
[76] P. Abbasi et al., Nano Letters **22** (2022) 4276–4284. [*CrossRef*]
[77] I. Derkaoui et al., Computational Materials Science **217** (2023) 111913. [*CrossRef*]
[78] K. Nishiguchi et al., arXiv:2506.09372 (2025). [*CrossRef*]
[79] M.C. Choi et al., npj Computational Materials **11** (2025) 221. [*CrossRef*]
[80] X. Sun et al., Frontiers in Physics **13** (2025) 1562239. [*CrossRef*]
[81] M.A. Ghebouli et al., Semiconductors **60** (2026) 61–78. [*CrossRef*]
[82] T.M. Inerbaev et al., RSC Advances **15** (2025) 5405–5412. [*CrossRef*]
[83] S.H. Wemple, Physical Review B **2** (1970) 2679. [*CrossRef*]
[84] M. Rizwan et al., Optik **211** (2020) 164611. [*CrossRef*]
[85] P. Xie et al., International Journal of Hydrogen Energy **44** (2019) 11695–11704. [*CrossRef*]
[86] M. Usman et al., Solid State Communications **355** (2022) 114920. [*CrossRef*]
[87] Y. Fo et al., New Journal of Chemistry **45** (2021) 8228–8239. [*CrossRef*]
[88] M. Wang et al., Journal of Solid State Chemistry **280** (2019) 121018. [*CrossRef*]
[89] W. Zulfiqar, S.M. Alay-e-Abbas, Materials Today Communications **32** (2022) 103867. [*CrossRef*]
[90] D.K. Bhat, H. Bantawal, U.S. Shenoy, Nanoscale Advances **2** (2020) 5688–5698. [*CrossRef*]
[91] T.M. Inerbaev et al., Molecules **29** (2024) 2707. [*CrossRef*]

[92] D. Ghercă et al., ACS Applied Materials & Interfaces **17** (2025) 30910–30923. [*CrossRef*]
[93] T.M. Inerbaev et al., Molecules **31** (2026) 2497. [*CrossRef*]
[94] Zh.Ye. Zakiyeva et al., Materials **19** (2026) 2336. [*CrossRef*]
[95] S. Chandrappa et al., ACS Applied Materials & Interfaces **16** (2024) 8763–8771. [*CrossRef*]
[96] P.I. Uma, U.S. Shenoy, D.K. Bhat, Applied Surface Science Advances **15** (2023) 100408. [*CrossRef*]
[97] S. Goumri-Said, M.B. Kanoun, Catalysts **12** (2022) 1672. [*CrossRef*]
[98] M.Q. Saadon, H.A. Miran, Papers in Physics **16** (2024) 160002. [*CrossRef*]
[99] Y. Wang et al., Molecules **29** (2024) 2250. [*CrossRef*]
[100] K. Boonpalit, N. Artrith, arXiv:2412.15452 (2024). [*CrossRef*]
[101] H. Qiu, M. Yang, H. Huang, ACS Applied Materials & Interfaces **17** (2025) 35396–35408. [*CrossRef*]
[102] R.K. Rohj et al., Frontiers in Chemistry **9** (2021) 682979. [*CrossRef*]
[103] E.K. Abdel-Khalek et al., Applied Physics A **131** (2025) 338. [*CrossRef*]
[104] H. Kacimi-Naciri et al., Ceramics International **51** (2025) 23801–23813. [*CrossRef*]
[105] M. Lamhani et al., Inorganic Chemistry **62** (2023) 13405–13418. [*CrossRef*]
[106] H. Bentour et al., Optical Materials **129** (2022) 112431. [*CrossRef*]
[107] Y. Wang et al., RSC Advances **10** (2020) 40117–40126. [*CrossRef*]
[108] Y. Qin et al., ACS Catalysis **11** (2021) 11429–11439. [*CrossRef*]
[109] K. Sun et al., Molecules **30** (2025) 2618. [*CrossRef*]
[110] A. Bouzaid, Y. Ziat, H. Belkhanchi, Materials **18** (2025) 4389. [*CrossRef*]
[111] K. Ogawa et al., Journal of the American Chemical Society **147** (2025) 23180–23191. [*CrossRef*]
[112] T. Takata et al., Nature **581** (2020) 411–414. [*CrossRef*]
[113] A. Ou-khouya et al., Chemical Physics **581** (2024) 112253. [*CrossRef*]
[114] M. Maraj et al., Materials Science in Semiconductor Processing **144** (2022) 106573. [*CrossRef*]
[115] N. Filipoiu et al., Nanotechnology **36** (2024) 075702. [*CrossRef*]
[116] R.I. Eglitis et al., Condensed Matter **7** (2022) 70. [*CrossRef*]
[117] X. Liu, E.Y. Tsymbal, K.M. Rabe, Physical Review B **97** (2018) 094107. [*CrossRef*]
[118] N.M. Caffrey et al., Physical Review Letters **109** (2012) 226803. [*CrossRef*]
[119] Z. Zhu et al., Solid-State Electronics **50** (2006) 1756–1760. [*CrossRef*]
[120] G. Chen et al., Chemical Engineering Journal **496** (2024) 154261. [*CrossRef*]
[121] D. Sharma et al., Applied Catalysis B: Environmental **189** (2016) 75–85. [*CrossRef*]
[122] F. Opoku et al., Chemical Physics Impact **6** (2023) 100236. [*CrossRef*]
[123] S. Ali et al., ECS Journal of Solid State Science and Technology **12** (2023) 054001. [*CrossRef*]
[124] Y. Wang et al., Journal of Applied Physics **139** (2026) 025301. [*CrossRef*]
[125] A.V. Krukau et al., The Journal of Chemical Physics **125** (2006) 224106. [*CrossRef*]
[126] G. Kabdrakhimova et al., Open Engineering **16** (2026) 20250160. [*CrossRef*]

[127] Z. Yuan et al., Ceramics International **50** (2024) 34890–34900. [*CrossRef*]